BNL-90854-2009-CP

Te Inclusions in CZT Detectors: New Method for Correcting their Adverse Effects

A.E. Bolotnikov, S. Babalola, G.S. Camarda, Y. Cui, S.U. Egarievwe, R. Hawrami, A. Hossain, G. Yang, and R.B. James

Presented at the 2009 IEEE Nuclear Science Symposium and Medical Imaging Conference
Orlando, Florida
October 25-31, 2009

December 2009

Nonproliferation and National Security Department
Detector Development and Testing Division

Brookhaven National Laboratory
P.O. Box 5000
Upton, NY 11973-5000
www.bnl.gov

DISCLAIMER

Te inclusions in CZT detectors: New Method for Correcting their Adverse Effects

A. E. Bolotnikov, *Member, IEEE*, S. Babalola, G. S. Camarda, Y. Cui, *Member, IEEE*, S. U. Egarievwe, R. Hawrami, A. Hossain, G. Yang, and R. B. James, *Fellow, IEEE*

***Abstract*—Both Te inclusions and point defects can trap the charge carriers generated by ionizing particles in CdZnTe (CZT) detectors. The amount of charge trapped by point defects is proportional to the carriers' drift time and can be corrected electronically. In the case of Te inclusions, the charge loss depends upon their random locations with respect to the electron cloud. Consequently, inclusions introduce fluctuations in the charge signals, which cannot be easily corrected. In this paper, we describe direct measurements of the cumulative effect of Te inclusions and its influence on the response of CZT detectors of different thicknesses and different sizes and concentrations of Te inclusions. We also discuss a means of partially correcting their adverse effects.**

***Index Terms*—CdZnTe, radiation detectors, crystal defects**

I. Introduction

Recent improvements in crystal growth opened an opportunity for making CZT detectors with greater effective areas [1-3]. Nevertheless, the availability of large-volume CZT detectors remains very limited. The main reason for this dearth is that today's commercial CZT material has excessively high concentrations of extended defects, such as twins, grain boundaries, dislocations, and Te inclusions that limit the performance and production yield of large-volume CZT detectors. Twins and grain boundaries entail significant charge losses, but since they are identified easily, detector-grade CZT crystals containing them can be rejected. In contrast, dislocation bands and Te inclusions trap smaller fractions of the charge from the electron clouds, but collectively, and over long drift-distances, they introduce significant fluctuations in the devices' responses. The exact mechanism of the charge trapping by inclusions is still debated. Our high-spatial-resolution X-ray scans indicate that Te inclusions effectively "block" electron transport (perhaps due to defects near the inclusion-bulk interface) and, in the first approximation, can be considered as 100% opaque to the electrons. Previously, we reported the numerical simulations of this effect predicting its strong dependence on the size and concentration of Te inclusions. These simulations relied on the experimental data obtained from high-spatial-resolution X-ray mapping of the charge loss caused by individual inclusions. Here, we present our direct measurements of the cumulative effect of Te inclusions of different sizes and concentrations in CZT detectors of various thicknesses.

Te inclusions, typically ranging from 1-20 um, form in CZT crystals during growth [4] and are easily identified by transmission IR microscopy. They differ from Te precipitates (typically in size 10-1000 nm) that result from the nucleation and coalescence of native defects [4]. Although the concentration of Te inclusions may exceed 10^7 cm^{-3}, this is several orders-of-magnitude less than that of the Te precipitates, $>10^{12}$ cm^{-3}, or point defects, $>10^{16}$ cm^{-3} [4]. Precipitates behave almost like point defects; the amount of lost charge depends solely on the carriers drift time and is described in terms of the $\mu\tau$-product. Since the fluctuations of the trapping are negligible, the total charge loss can be compensated by measuring electron drift times.

Using a highly collimated X-ray beam [5-7], the effect of charge trapping by individual inclusions is seen as reduction of output signals in comparison to a normal response. We developed a model [8,9] that correctly reproduces the effects of the individual Te inclusions revealed with these X-ray raster-scans. The model rests on the fact that the electron's mean-free-path is much smaller than the typical diameter of Te inclusions. Therefore, we can describe the carriers' transport as a drift-diffusion process in a discontinuous medium filled with Te inclusions. Each interaction of the electron cloud with a Te inclusion entails a certain amount of charge loss proportional to the number of electrons crossing the inclusion's geometrical area; that is, it is contingent upon the mutual locations of the inclusions and the center of the electron cloud. The model depends on a single adjustable parameter, viz., the ratio between the effective diameters of Te

Manuscript received October 27, 2009. This work was supported by U.S. Department of Energy, Office of Nonproliferation Research and Development, NA-22 and Defense Threat Reduction Agency. The manuscript has been authored by Brookhaven Science Associates, LLC under Contract No. DE-AC02-98CH1-886 with the U.S. Department of Energy.

A. E. Bolotnikov, G. S. Camarda, Y. Cui, A. Hossain, G. Yang, and R. B. James are with Brookhaven National Laboratory, Upton, NY 11793 USA (phone: 631-344-8014; e-mail: bolotnik@bnl.gov).

S. Babalola is with Fisk University, Nashville, TN 37208, USA and Vanderbilt University, Nashville, TN 37235, USA.

S. U. Egarievwe is currently with Alabama A&M University, Normal, AL 35752, USA.

R. Hawrami is currently with Radiation Monitoring Devices, Inc., Watertown, MA 02472, USA.

inclusions and the actual ones obtained from IR microscopy measurements [9]. Using as input parameters the size distributions and concentrations of Te inclusions obtained from IR microscopy, we simulated the total collected charge and its fluctuations due to the random distribution of interaction points inside the detector.

To verify our model we developed an experimental technique that allowed us to measure directly the cumulative effect of different distributions of Te inclusions on the spectral responses of CZT detectors of distinct thicknesses. In this technique, we employed a highly collimated X-ray beam to obtain the detector response map which allows us to evaluate the detector response functions. The peak width of the response function, free from contribution of electronic noise, is a measure of the device response uniformity and can be used to evaluate directly the cumulative effect of Te inclusions.

In these studies, we selected CZT detectors in which Te inclusions play dominant roles and constitute the primary cause of the energy resolution degradation. The micron-scale X-ray mapping allows us to select the samples without other potentially present extended defects, such as grain boundaries or extensive dislocation bands. Te inclusions are represented by the round dark spots in the X-ray response maps that can be used to distinguish them from other types of defects, e.g., boundaries or dislocations bands, which are typically seen as linear features. This approach ensures that the peak width of the response function is governed by the effect of Te inclusions only.

II. Experimental

We employed a high spatial resolution X-ray mapping system [10] at BNL's National Synchrotron Light Source (NSLS) to generate response maps from the CZT detectors with the resolution determined by the 20-, 25-, or 50-μm step sizes. Here, the step sizes used depend on the scanned area. For example, large-area detectors were scanned with 50-μm steps to reduce the measurement time.

We evaluated six CZT detectors of different thicknesses and distributions of Te inclusions summarized in Table 1. The detectors were acquired from different vendors and all had high $\mu\tau$-products >$7x10^{-3}$ cm^2/V.

The detector under test was placed inside a standard eV-Products' holder and mounted on an X-Y translation stage. For each position of the X-ray beam, we collected a pulse-height spectrum and fitted its peak parameters by using a Gaussian function. With typical peak maxima at a channel of ~100, and fitting errors in the range of 0.4-0.7 channel (depending on the statistics), the accuracy of the peak-position evaluation was <0.7% even though the typical width of the peak itself was 10-20 channels, mostly determined by electronic noise. A peak's channel number represents the signal's amplitude, which is proportional to the total collected charge generated within a beam's spot area: ~10x10 μm^2. The distribution of the peak's channels over the device's area represents the detector's response map, from which we can generate the frequency distribution of the peaks' positions, also called the detector's response function. It represents a pulse-height spectrum that X-rays uniformly illuminating the device surface would generate. The width of this distribution reflects the variation of the collected charge with no contributions of electronic noise and of the electron-hole pair production statistics. In other words, the width of the response function sets a lower limit on the detector's spectral resolution.

Te inclusions introduced small-scale variations in the device response. Thus their cumulative effect should saturate over an area much greater that the size of the electron cloud. Our simulations [9] indicate that the broadening of the response function due to inclusions saturates above ~1x1-mm^2 area for a 10-mm- thick device. On the other hand, the broadening of the response function can also arise from large-scale gradual changes in the $\mu\tau$-product caused by nonuniform distributions of the point defects inside the crystal. To exclude a potential contribution of large-scale variations, we divided the response maps into 1x1-mm^2 segments (pixels) and normalized them before combining the overall response function. The normalization procedure is identical to the signal correction in pixel detectors. The peak positions evaluated for the individual pixels are equalized by introducing the scaling coefficients which are then applied to correct the overall response map and function. The peak widths (%FWHM) evaluated for the normalized response functions are presented in Table 1. It should be mentioned that in this work we used ~30-keV X-rays, all absorbed near the cathode, to evaluate the response functions which are differ from those expected from gamma rays that can interact at any point inside the detector. However, since the electron clouds generated near the cathode travel across the device's entire thickness, they are sensitive to all defects inside a crystal, and, thus, can also be used to characterize the detector's performance in the case of gamma rays.

By taking a series of images at different focal lengths (or at different depths) using our IR-transmission microscopy system, described elsewhere [7], we obtained volumetric images of Te inclusions inside the crystals and evaluated their size distributions and concentrations. Fig. 1 shows the projections of the volumetric images on the plane perpendicular to the directions at which we took the images. Each image represents the inclusions inside a 1x1 mm^2 area.

TABLE 1
CHARACTERISTICS OF CZT DETECTORS USED

Detector's number	D1	D2	D3	D4	D5	D6
Dimensions, mm^3	10x10x1.5	10x10x5	5x5x12	6x6x15	20x20x15	10x10x10

Total concentration of inclusions, cm^{-3}	$1.1x10^5$	$5.3x10^5$	$4.5\ x10^5$	$6.6\ x10^5$	$7.2\ x10^5$	$4.9\ x10^5$
Concentration of Te inclusions with diameters >10 μm, cm^{-3}	$2.1x10^4$	$3.8x10^4$	$1.4x10^3$	$2.1x10^2$	$1.4x10^4$	$1.7x10^4$
Width of response function, % FWHM	0.6	1.7	0.9	0.3	3.7	3.4

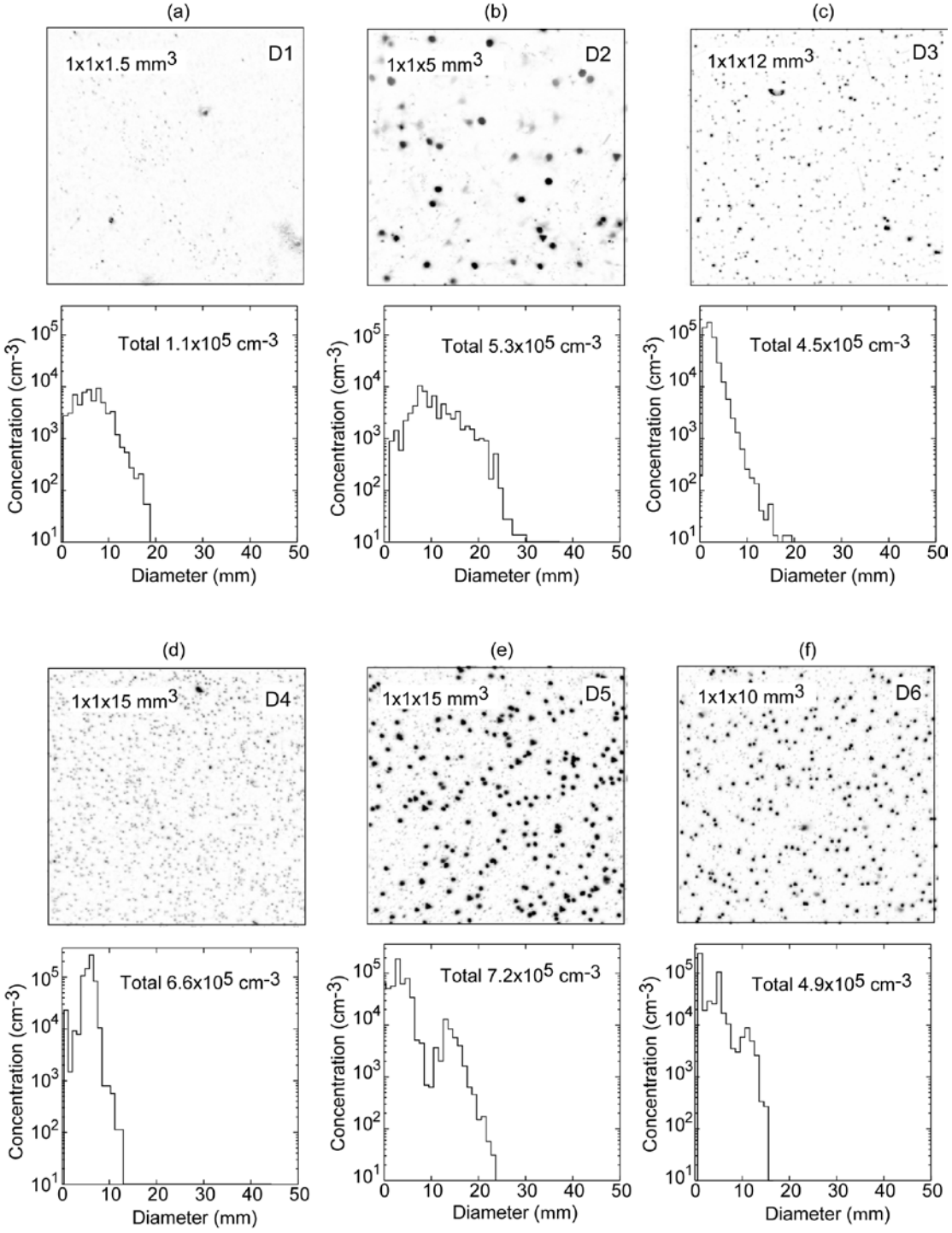

Fig. 1. IR images of the Te inclusions (top) and their size distributions averaged over the six crystals' volumes (bottom). Each image shows the inclusions within a rectangular region of 1x1 mm^2 and length equal to the detector's width, projected on the same plane.

The corresponding size distributions of Te inclusions are displayed below the images.

As shown in Table 1, we measured similar total concentrations of Te inclusions with typical magnitudes of (5-7) $x10^5$ cm^{-3} for all the samples, except for the 1.5-mm thin detector, D1. However, the size distributions were found to be different as shown in Fig. 1. Detectors D3 and D4 mostly have small, 3-5 μm, inclusions, while the distribution in the rest of the detectors shifted towards larger sizes. For further evaluations, we divided the inclusions into two size categories; small, <5 μm, and big, >10 μm. We chose these two regions of inclusion sizes based on our simulations that predict inclusions with diameters below 5 μm have a small effect on the energy resolution (after the charge loss correction), while inclusions with diameters above 10 μm are especially harmful for the device performance. As is apparent in Table 1, the concentration of big inclusions in detectors D3 and D4 is about one order-of-magnitude less than that in the other detectors. Even though detectors D3 and D4 have large thickness, they showed the best spectral responses, which we attribute to the small concentrations of big Te inclusions in these samples.

III. Results and Discussion

A. The case of a thin detector with big Te inclusions

Figure 2 shows the raster-scan map and response function measured for the thin, 1.5-mm, detector D1 with a low concentration of small Te inclusions but high concentration of big ones. This response map (a) was collected at a 200-V cathode bias with 20-μm steps in both directions. The dark spots in the map represent low-output signal areas corresponding to the big Te inclusions that appear as sharp peaks in the isometric representations (b) of the original (top) and inverted (bottom) response maps. Note that we plotted the area of the marked square that is free from edge effects.

Two histograms (c) and (d) represent the frequency distribution of peak positions (the detector's response function) evaluated for the marked area and plotted in normal- and semi-logarithmic- coordinates. The distribution has a very narrow peak whose width, <0.6% FWHM, we attribute entirely to the fitting errors of the original pulse-height spectra. This example verifies that Te inclusions have a negligible effect on the energy resolution in such thin detectors. However, they affect the device's photopeak efficiency. When an interaction occurs just above the Te inclusions, a significant charge loss from the electron cloud ensues. Such events contribute to the low-energy tail, causing a reduction of the photopeak efficiency, as is evident in the spectrum plotted in semi-logarithmic coordinates (d).

B. The case of a medium-thickness detector with big Te inclusions

Figure 3 depicts the results obtained from the 5-mm thick detector, D2, with a high concentration of big inclusions (similar to detector D1). The response map (a) was measured with 50-μm steps and at a 1000-V cathode bias in this case. Again, the dark spots represent low-output signal areas corresponding to the Te inclusions that also appear as sharp peaks in the isometric representations (b) of the original- (top) and inverted-(bottom) response maps. No other extended defects are visible in them. As before, we selected the marked area free from edge effects to assess the frequency distribution of peak positions (c). In contrast to the thin detector for which the histogram had a very narrow peak, the distribution here has a much broader

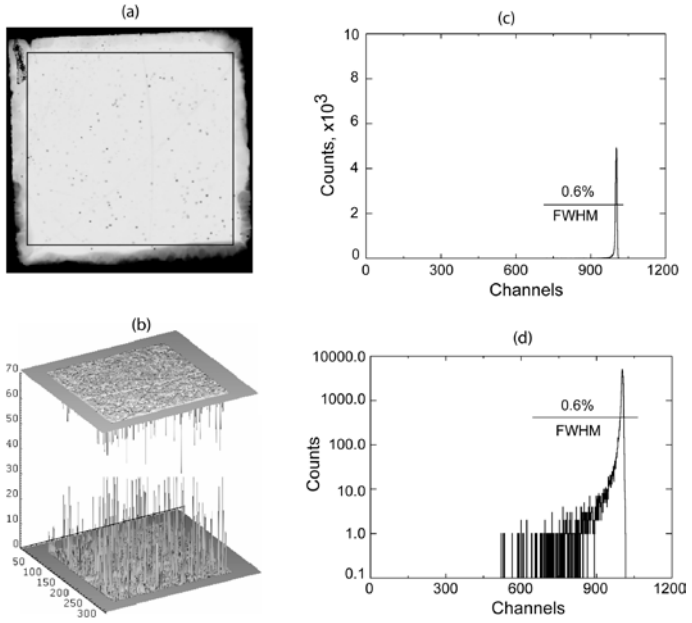

Fig. 2. The raster-scan map shown as 2-dimensional (a) and isometric (b) plots, and the frequency distribution of the peaks' positions (the detector's response function) evaluated for the marked area and plotted in the normal (c) and semi-logarithmic (d) coordinates for detector D1, 10x10x1.5 mm^3, with a low

concentration of small Te inclusions but high concentration of big ones. The response map was acquired at a 200-V cathode bias with 20-µm steps in both directions.

asymmetric peak of 1.9% FWHM width. To exclude a potential effect due to large-scale variations of the $\mu\tau$-product, we divided the response maps into 1x1 mm^2 areas and normalized their responses before plotting the overall histogram. This procedure is equivalent to implementing a pixel-readout scheme to correct for non-uniformities in CZT material. Accordingly, the width of the response function slightly improves to 1.7%, as evident in Fig. 3(c). As we mentioned earlier, we expect the magnitude of the fluctuations caused by Te inclusions to saturate over an area of >1x1 mm^2. Thus, we attribute the 1.7% FWHM to the Te inclusions whose effect increases with the device's thickness in comparison to D1.

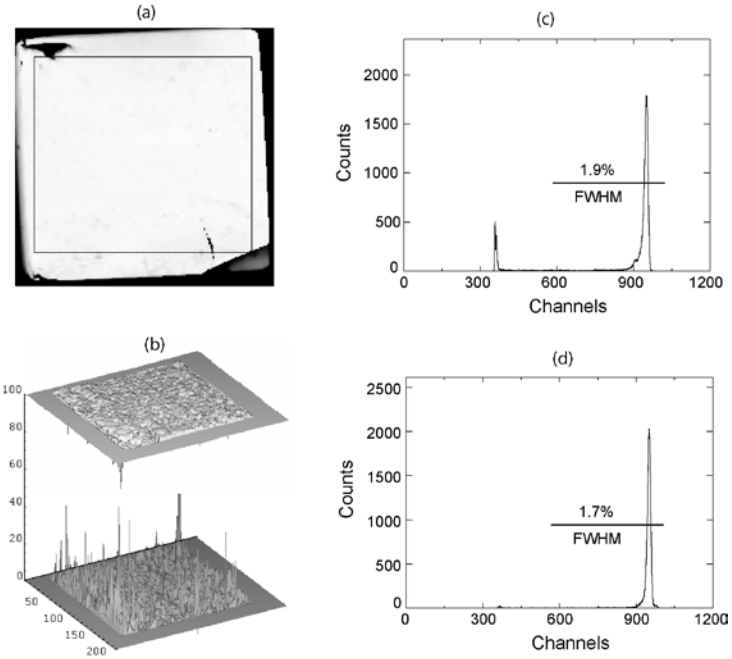

Fig. 3. The raster-scan map shown as 2-dimensional (a) and isometric (b) plots, and the detector's response function evaluated for the marked area before (c) and after (d) applying the normalization procedure to the detector D2, 10x10x5 mm^3, with a high concentration of big Te inclusions. The response map was measured with 50-µm steps in both directions at a 1000-V cathode bias. During the normalization procedure, the total response map was divided into 1x1-mm^2 pixels and gain corrections were introduced to equalize the peak positions for each pixel. Then, the overall response function was re-evaluated.

C. The case of a low concentration of big Te inclusions

Figures 4 and 5, respectively, illustrate the results obtained for the parallepiped 12- and 15-mm thick detectors, D3 and D4, with low concentrations of big Te inclusions. The response maps, shown as 2-dimensional (a) and isometric (b) plots, were measured with 25-µm steps and at a 1700- and 2000-V cathode bias for the detectors D3 and D4, correspondingly. The peak's width of the frequency distributions evaluated for the entire area of the detector D3 was 1.3% FWHM. After dividing the response map into 1x1 mm^2 areas, and applying a normalization procedure, the ensuing width fell to 0.9% (d). Further segmentation to a pixel size of 0.5x0.5 mm^2 reduced the width close to its statistical limit of 0.7%. The width of the frequency distributions evaluated for the detector D4 (Fig. 5(c)) was only 0.4% FWHM. Despite its large thickness, this detector exhibits the best performance with a high-uniformity response map; after the normalization procedure, the width decreased to 0.3%. These results indicate that Te inclusions have little or no effect on the energy resolution in these particular devices with low concentrations of big inclusions. Nonetheless, plotting the response functions of both detectors on a semilogarithmic scale (c) reveals low-energy tails that point to reductions of photopeak efficiencies similar to those described in the previous cases.

D. The case of large thickness detectors with high concentrations of big Te inclusions

Figure 6 shows the results obtained for the 15-mm thick detector, D5, with a high concentration of big Te inclusions. The response map was measured with 50-µm steps at 1500-V cathode bias. As in previous cases, the dark spots in the raster-scan map (a) represent low-output signal areas corresponding to the Te inclusions, also seen as sharp peaks in the isometric representation (c). We generated additional raster-scan maps (b) by applying an adaptive histogram-equalization filter [11] to enhance low-intensity features in the image. The peak's width of the frequency distributions evaluated for the entire

area of the detectors (d) was 4.9% FWHM. After dividing the response map into 1x1 mm^2 areas and applying a normalization procedure, the width was slightly reduced to 3.7% (d). Since this response map was obtained with 50-µm steps, further segmentation would not be statistically valid. Detector D5 undoubtedly represents an extreme case of a CZT crystal with a high concentration of large Te inclusions. In addition, this detector's considerable thickness enhanced the resulting fluctuations in the collected charge. Figs. 7 and 8 display the results from the 10-mm thick detector, D6, also with a high concentration of big Te inclusions. The response map shown in Figs. 7 (a-c) was measured with 25-µm steps at 1000-V cathode bias. As evident in the response map (a), detector D6 has a twin boundary that effectively splits the device into two sections with different responses. The map (b) was generated by applying an adaptive histogram-equalization filter to enhance the faded features. Figs. 8 (a-e) show the response functions evaluated for the detector D6. The peak's width of the frequency distributions evaluated for the entire area of the detector after excluding the region around the twin (upper region) was 4.8% (b).

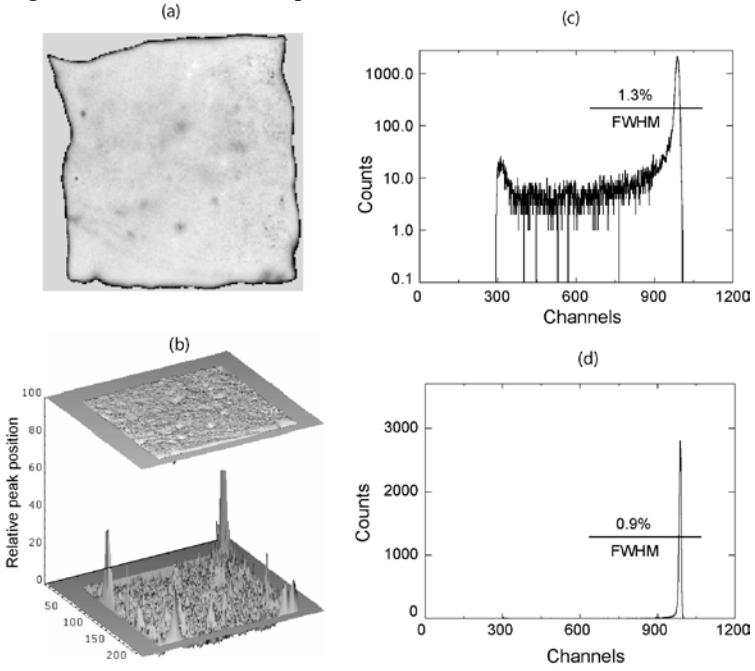

Fig. 4. The raster-scan map, shown as 2-dimensional (a) and isometric (b) plots, and the response function evaluated before (c) and after (d) applying the normalization procedure to detector D3, 5x5x12 mm^3, with a low concentration of big Te inclusions. The response map was measured with 25-µm steps in both directions at a 1700-V cathode bias. The normalization procedure is the same as in Fig. 3.

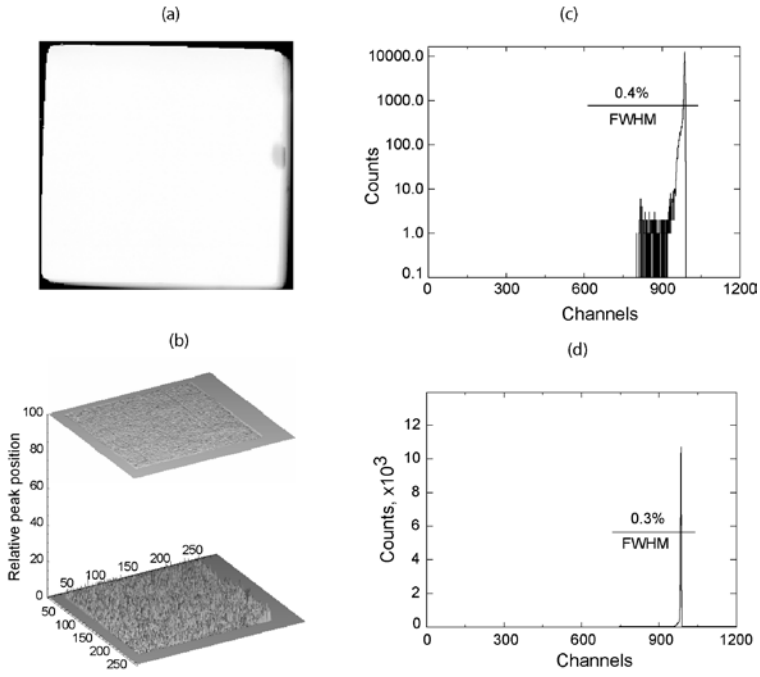

Fig. 5. The raster-scan map, shown as 2-dimensional (a) and isometric (b) plots and the response function evaluated before (c) and after (d) applying the normalization procedure of the detector D4, 6x6x15 mm^3, with a low concentration of big Te inclusions. The response map was measured with 25-μm steps in both directions at a 2000-V cathode bias. The normalization procedure is the same as in Fig. 3.

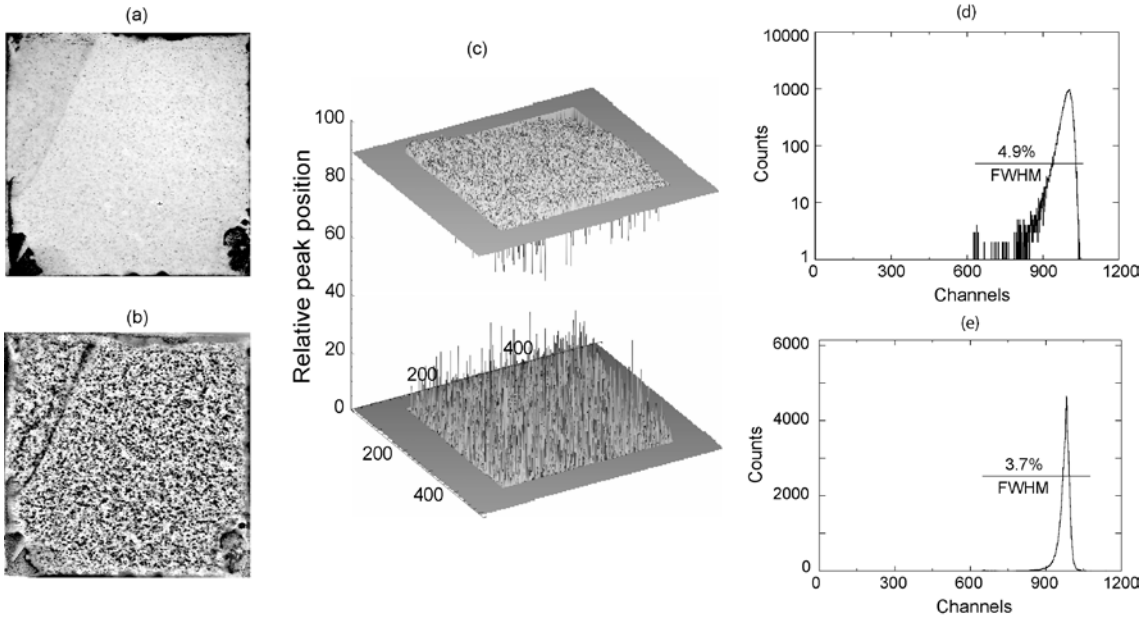

Fig. 6. The raster-scan map, shown as 2-dimensional (a, b) and isometric (c) plots, and the response function evaluated before (d) and after (e) the normalization of detector D5, 20x20x15 mm^3, with a high concentration of big Te inclusions. The raster-scan was carried out with 50-μm steps and at a 1500-V cathode bias. Map (b) was generated by applying an adaptive histogram-equalization filter to enhance small faded features. The normalization procedure is the same as in Fig. 3.

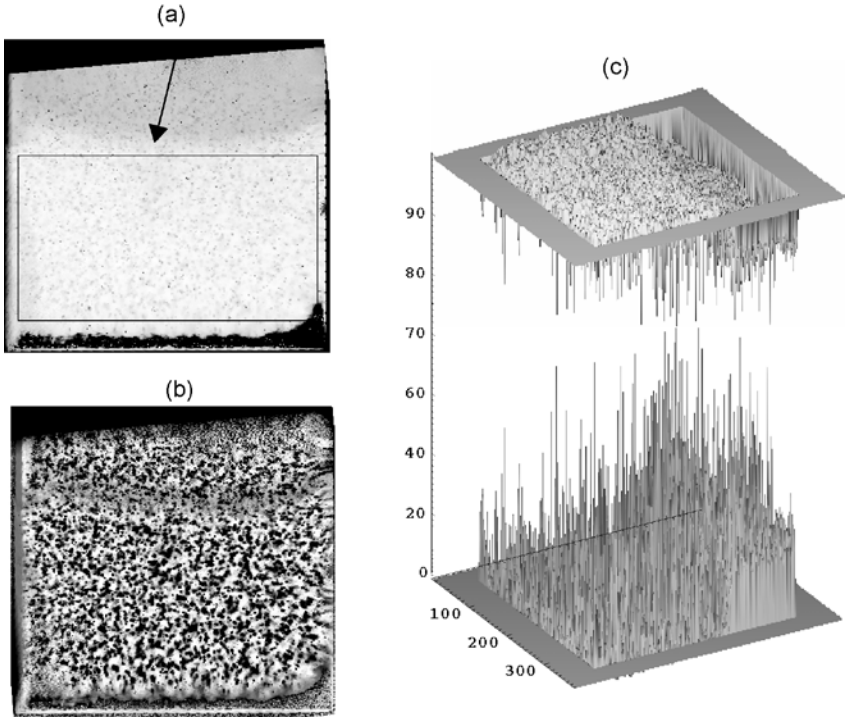

Fig. 7. The raster-scan map of the detector D6, 10x10x10 mm^3, with a high concentration of big Te inclusions. A response map was measured with 25-μm steps and at a 1000-V cathode bias. The map (b) was generated by applying an adaptive histogram-equalization filter to enhance the faded features. The arrow indicates a location of the twin boundary.

E. Correcting small-scale variations caused by Te inclusions

We used detector D6 to illustrate the application of response-function segmentation to correct small-scale variations caused by Te inclusions because its response map was measured with high spatial resolution, 25 μm, and large statistics, which allowed us to reduce the segment size during renormalization down to 0.1x0.1 mm^2. We plotted the corresponding response functions of detector D6 in Fig. 8 (a-f). The response function of the entire area of the detector (a) contains two broad peaks corresponding to the two parts of the detector divided by the twin boundary. Since we are primarily concerned with the effects of Te inclusions, for further analysis, we excluded the upper portion of the map with a low response. Fig. 8 (b) shows the response function, evaluated for the selected area, with its peak width of ~4.8%. As discussed above, this width could be caused in part by the large-scale gradual variations in the detector's response. After dividing the response map into 1x1 mm^2 areas and applying the normalization procedure, the peak width fell to 3.4% (c). We attribute this value entirely to the fluctuation caused by Te inclusions. Figs. 8 (d), (e), and (f), respectively, show the corrected response functions evaluated after further segmenting the original response map into 0.5x0.5, 0.15x0.15 and 0.1x0.1 mm^2 areas. Although a small improvement in the peak's width is attained when pixel size decreases from 1 mm to 0.5 mm (d), lowering pixel size to 0.1 mm (e) and (f) brought about a major improvement. The peak widths were 1.8% and 1.2%, respectively, for the 0.15- and 0.1-mm pixel size.

In the above example, we normalized the detector's response function measured with a highly collimated X-ray beam. It also illustrates that the same improvements of the CZT detector spectral response can be achieved with the position sensitive (pixel) detectors. By reading signals from several adjacent pixels and from the cathode, it is possible to locate origins of the electron clouds within areas of ~100x100 μm^2 or smaller (depending on a pixel size) in x-y directions and ~500 μm in the z direction [12,13]. This allows one to calibrate and correct the response from each voxel of the CZT crystal including the deviations caused by Te inclusions. To illustrate this, we simulated pulse-high spectra that would be expected from detector D6. We "flood illuminated" the detector with 30-keV photons from the cathode side to mimic the results of the X-ray scan shown in Fig. 8. We assumed an ideal detector with no charge lost other than due to Te inclusions. For simplicity we assumed that inclusions had the same average diameter of 13 μm and a concentration of $2x10^4$ cm^{-3}. This value corresponds to the concentration of Te inclusions with sizes >10 μm found in the sample D6 (Table 1). The particular diameter of 13 μm was chosen to match the peak width of the simulated spectra to that in the measured response function of the detector D6 after the correction for large-scale variations (Fig.8(c)).

We modeled [8,9] electron transport and trapping as a drift-diffusion process in a discontinuous medium filled with ball-like inclusions assumed to be opaque to the electron cloud. Fig. 9 shows simulated pulse-height spectra after corrections for different voxel sizes: 1, 0.5, 0.15, 0.1, 0.05, and 0.025 mm. These should be compared with the corresponding spectra presented in Fig. 8. The model predicts the same trend as observed in the experiment, that is, anode segmentation helps to overcome the effect of the small-scale extended defects such as Te inclusions. In the first approximation, the modeled spectra are similar to the measured ones and show similar improvement of the energy resolution when the voxel size is reduced. This supports our interpretation that fluctuations caused by Te inclusions is the main factor determining the peak widths in the measured response functions, and they can be corrected by using high-granularity position sensitive detectors. The discrepancies between measured and simulated spectra for small pixel sizes, < 0.5 mm, should be attributed to the assumptions within the simulations, such as a distribution of inclusions with the same size, and to the statistical fluctuations resulted from the relatively large step size (25 μm) used in the scan.

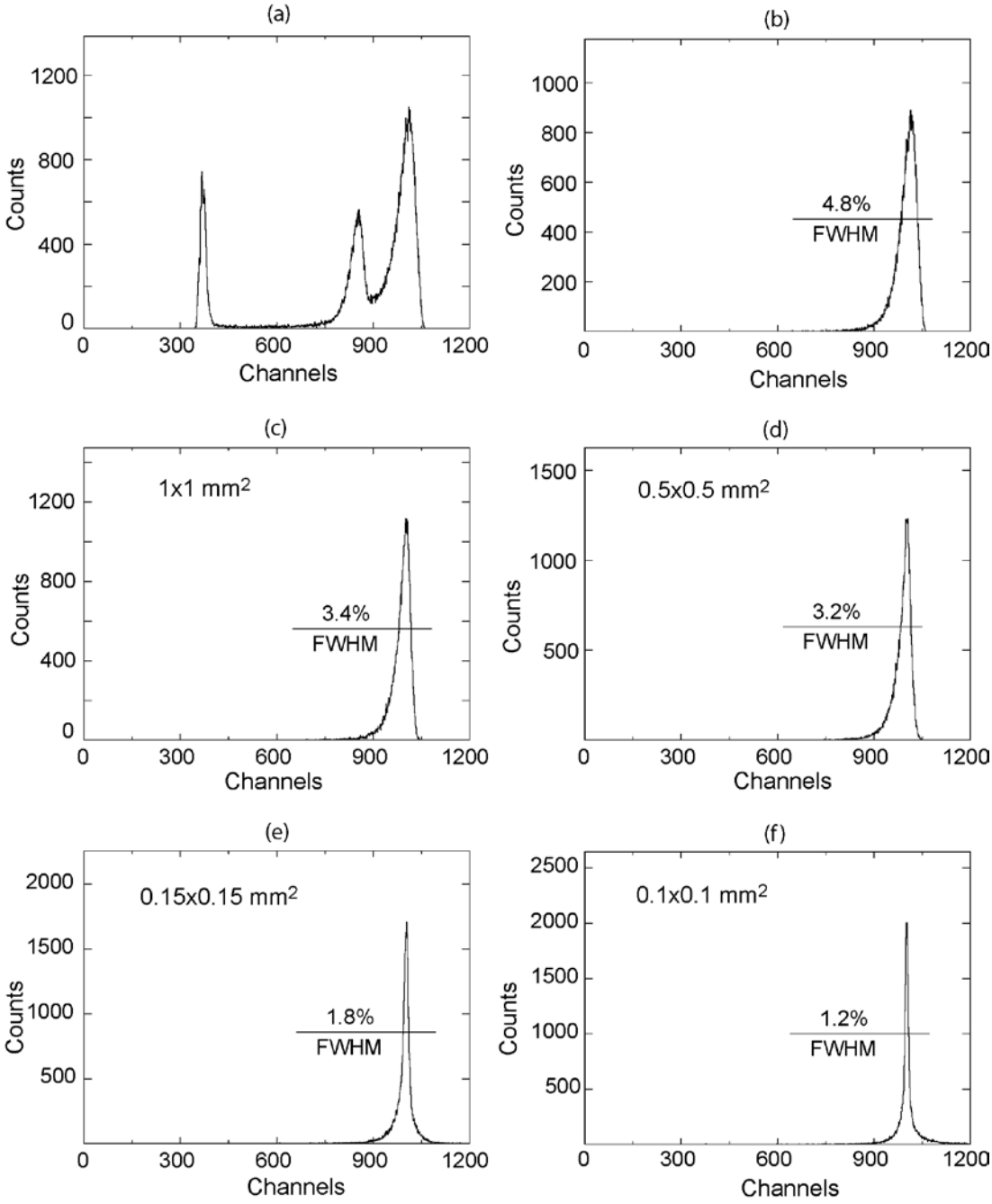

Fig. 8. The response functions evaluated for the detector D6: (a) and (b) the whole area and the selected one before corrections; (c)-(f) the selected area after corrections, pixel size 1x1, 0.5x0.5, 0.15x0.15, and 0.1x0.1 mm^2, correspondingly.

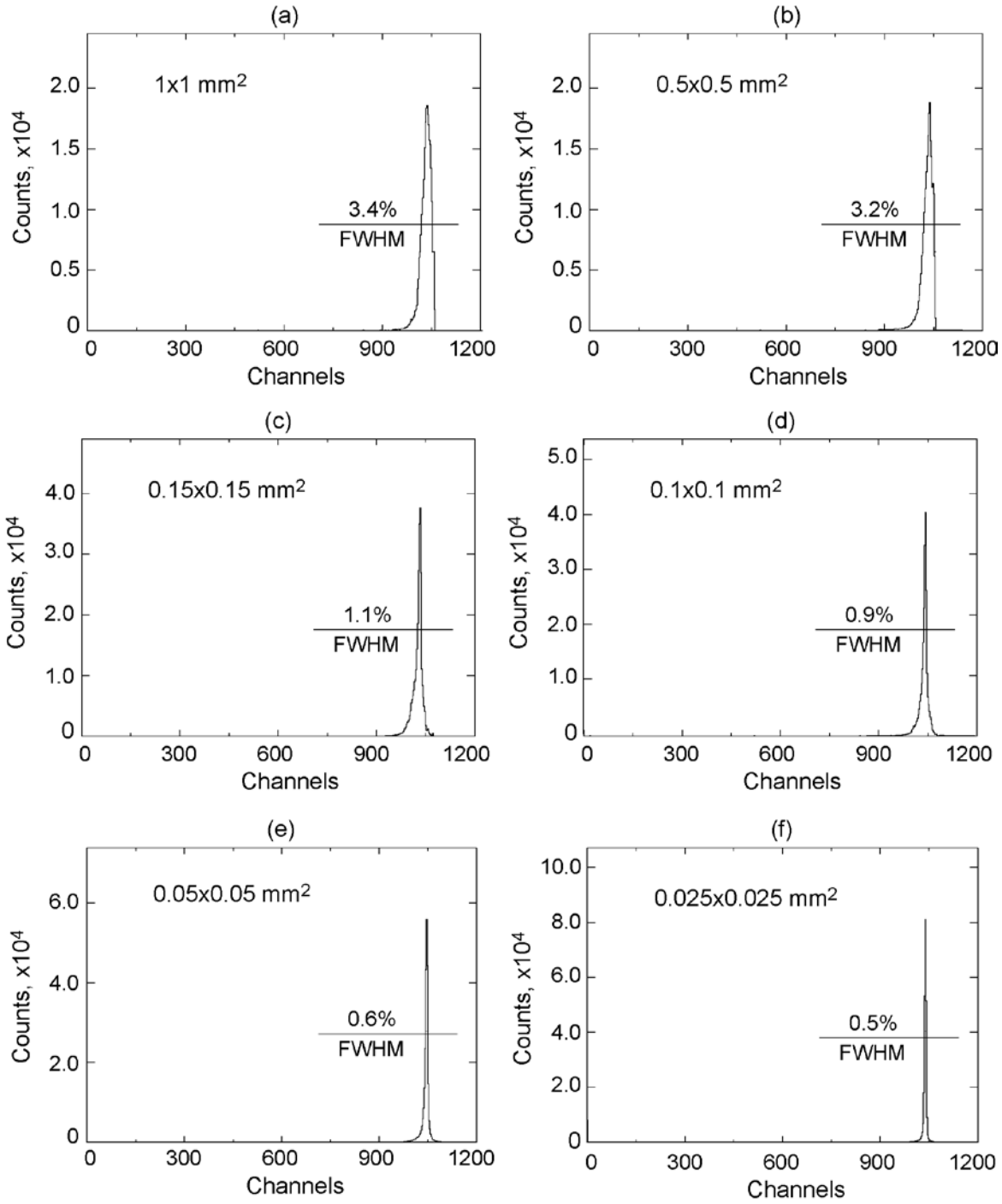

Fig. 9. The simulated pulse-height spectra for the detector D6 assuming that all the inclusions had the same "average" diameter of 13 μm and a concentration of $2x10^4$ cm^{-3}. The voxel size is 1x1, 0.5x0.5, 0.15x0.15, 0.1x0.1, 0.05x0.0x, and 0.025x0.025 mm^2, correspondingly.

An interesting feature is the presence of the tails on both sides of the peaks in the corrected response functions depicted in Figs. 8 (e) and (f) and Figs. 9 (c) and (d). These tails have the same origin as the low-energy tail seen in Fig. 2 (d), i.e., due to incomplete charge collection. Similar tails usually exist in pulse-height spectra measured with pixel detectors employing a 3D correction technique [12]. Now we know that Te inclusions primarily are responsible for them. Depending on the size and concentration of Te inclusions, such tails may encompass a substantial fraction of the events (relative to the events under the peak), thereby lowering the detector's photopeak efficiency.

IV. Conclusions

We demonstrated experimentally the cumulative effect of Te inclusions on the energy resolution and detection efficiency of CZT detectors. The variations in the charge trapped by the Te inclusions due to the random distribution of the interaction

points over the device's volume can introduce significant fluctuations in the responses of thick CZT detectors, and ultimately degrade their performance. The criticality of the role of inclusions depends on their size distributions and the device's thickness.

We presented examples of two size distributions of Te inclusions, one resulting in little response broadening and the other significantly increasing it.

We also showed that small-scale variations in the collected charge caused by Te inclusions can be reduced by segmenting the detectors, and applying a charge-correction scheme, thus affording a new method to mitigate material deficiencies in CZT.

REFERENCES

[1] C. Szeles, "Advances in the Crystal Growth and Device Fabrication Technology of CdZnTe Room Temperature Radiation Detectors", IEEE Trans. Nucl. Sci. 51, n. 3, pp. 1242-1249, 2004.

[2] H. Chen, S. A. Awadalla, K. Iniewski, P. H. Lu, F. Harris, J. Mackenzie, T. Hasanen, W. Chen, R. Redden, G. Bindley, I. Kuvvetli, C. Budtz-Jørgensen, P. Luke, M. Amman, and J. S. Lee, "Characterization of large cadmium zinc telluride crystals grown by traveling heater method," J. Appl. Phys. 103, pp. 014903, 2008.

[3] L. Li, F. Lu, K. Shah, M. Squillante, L. Cirignano, W. Yao, R. W. Olson, P. Luke, Y. Nemirovsky, A. Burger, G. Wright, and R. B. James, "A new method for growing detector-grade cadmium zinc telluride crystals" Nuclear Science Symposium Conference Record, 2001 IEEE, v. 4, n. 4-10, pp. 2396-2400, 2001.

[4] P. Rudolph, Non-stoichiometry related defects at the melt growth of semiconductor compound crystals – a review", Cryst. Res. Technol. 38, n. 7-8, pp. 542-554, 2003.

[5] G. A. Carini, A. E. Bolotnikov, G. S. Camarda, G. W. Wright, L. Li, and R. B. James, "Effect of Te inclusions on the performance of CdZnTe detectors", Appl. Phys. Lett. 88, p. 143515, 2006.

[6] G. S. Camarda, A. E. Bolotnikov, G. A. Carini, and R. B. James, "Effects of Tellurium Inclusions on charge collection in CZT Nuclear Radiation Detectors", in Countering Nuclear and Radiological Terrorism, edited by S. Aprkyan and D. Diamond, Springer, 2006, pp. 199-207.

[7] A. E. Bolotnikov, G. S. Camarda, Y. Cui, K. T. Kohman, L. Li, M. B. Salomon, and R. B. James, "Performance-Limiting Defects in CdZnTe Detectors", IEEE Trans. Nucl. Sci. 54, pp. 821-827, 2007.

[8] A. E. Bolotnikov, G. S. Camarda, G. A. Carini, Y. Cui, L. Li, and R. B. James, "Modeling the geometrical effects of Te precipitates on electron transport in CdZnTe", Nucl. Instr. Meth. A579, pp. 125–129, 2007.

[9] A. E. Bolotnikov, G. S. Camarda, G. A. Carini, Y. Cui, L. Li and R. B. James, "Cumulative Effects of Te Precipitates in CdZnTe Radiation Detectors", Nucl. Instr. and Meth. A571, pp. 687-698, 2007.

[10] G. S. Camarda, N. M. Abdul-Jabbar, S. Babalola, A. E. Bolotnikov, Y. Cui, A. Hossain, E. Jackson, H. Jackson, J. R. James, A. L. Luryi, M. Groza, A. Burger, and R. B. James, "Characterization and Measurements of CZT Material: Novel Techniques and Results", in Proceedings of SPIE Hard X-Ray and Gamma-Ray Detector Physics IX, Vol. 6706, edited by R. B. James, A. Burger and L. A. Franks (SPIE, Bellingham, WA, 2007), 670605.

[11] S. Pizer et. al., "Adaptive Histogram Equalization and its Variations", Computer Vision, Graphics and Image Processing, Vol. 39, pp. 355-368, 1987.

[12] F. Zhang, Z. He, G. F. Knoll, D. K. Wehe, and J. E. Berry, "3-D position sensitive CdZnTe spectrometer performance using third generation VAS/TAT readout electronics", IEEE Trans. Nucl. Sci. 52(5), pp. 2009-2016, 2005.

[13] S. Procz, J. Lubke, A. Zwerger, M. Mix, and M. Fiederle, "Optimization of Medipix-2 threshold mask for spectroscopic x-ray imaging", IEEE Trans. Nucl. Sci. 56(4), pp. 1795-1799, 2009.